

Interplay of electronic, structural and magnetic properties as the driving feature of high-entropy CoCrFeNiPd alloys

This content has been downloaded from IOPscience. Please scroll down to see the full text.

2017 J. Phys. D: Appl. Phys. 50 185002

(<http://iopscience.iop.org/0022-3727/50/18/185002>)

View [the table of contents for this issue](#), or go to the [journal homepage](#) for more

Download details:

IP Address: 129.67.246.57

This content was downloaded on 03/04/2017 at 16:25

Please note that [terms and conditions apply](#).

Interplay of electronic, structural and magnetic properties as the driving feature of high-entropy CoCrFeNiPd alloys

M Calvo-Dahlborg¹, J Cornide¹, J Tobola², D Nguyen-Manh³, J S Wróbel^{3,4}, J Juraszek¹, S Jouen¹ and U Dahlborg¹

¹ Groupe de Physique des Matériaux, UFR des Sciences de l'Université Rouen Normandie, Avenue de l'Université, 76801 Saint Etienne du Rouvray, France

² Faculty of Physics and Applied Computer Science, AGH University of Science and Technology, al. Mickiewicza 30, 30-059 Kraków, Poland

³ Culham Centre for Fusion Energy, Culham Science Centre, Abingdon, Oxfordshire, OX14 3DB, United Kingdom

⁴ Faculty of Materials Science and Engineering, Warsaw University of Technology, ul. Wołoska 141, 02-507 Warszawa, Poland

E-mail: monique.calvo-dahlborg@univ-rouen.fr

Received 17 November 2016, revised 10 February 2017

Accepted for publication 24 February 2017

Published 3 April 2017



Abstract

The structural and magnetic properties of CoCrFe_yNi and CoCrFeNi-Pd_x alloys earlier investigated experimentally by x-ray and neutron diffraction techniques and magnetometry have been theoretically reproduced using two complementary approaches for electronic structure calculations, i.e. the Korringa–Kohn–Rostoker method with the coherent potential approximation (KKR-CPA) and implemented in the *ab initio* framework of density functional theory and the Vienna *ab initio* simulation package (VASP) for supercell models of high-entropy alloy (HEA) structures. The comparison between experimental results and calculations of the lattice constants by both calculation methods indicate that the structure of CoCrFe_yNi is well described by ordered fcc configurations. The values of local magnetic moments on Fe, Co, Cr, and Ni atoms depend not only on the Pd concentration but on chemical disordering. In the case of the CoCrFeNi-Pd_x alloys, the KKR-CPA and the VASP calculations of disordered configurations reproduce the experimental values at 5 K up to equimolar composition and at 300 K above. The experimental values above the equimolar composition at 5 K are not satisfactorily reproduced by any of the calculations. The divergence between the experimental and calculated values is related to the variation of the ferromagnetic to paramagnetic transition temperature as a function of palladium content and to the existence of several phases, FeCoCr-rich above room temperature and FeCrPd-rich below, observed by diffraction and detected by microscopy and atom probe investigations. VASP calculations of a FeCrPd-rich phase effectively reproduced both the lattice constant and magnetization of the alloy above equimolar composition. An important conclusion of this work is that the combined analysis of the electronic, structural, and magnetic properties plays an important role in understanding the complexity of magnetic HEAs.

Keywords: high-entropy alloys, structure, magnetization, DFT, KKR-CPA, phases

 Supplementary material for this article is available [online](#)

(Some figures may appear in colour only in the online journal)

1. Introduction

Multicomponent high-entropy alloys (HEAs) have recently attracted considerable attention, because of their attractive physical properties such as ductility, irradiation resistance, hardness, high-temperature strength [1, 2], and superconductivity [3, 4]. According to the first bibliographic reports, an HEA was originally defined as an alloy consisting of five or more components of relative composition in the range 5 at.%–35 at.% forming single and simple close-packed crystalline structures of solid solution type [5, 6]. Much work has been undertaken in order to understand the formation of this new kind of alloy in terms of entropy and enthalpy of mixing, the electronegativity and concentration of valence electrons of the constituent elements, their atomic radii, and the resulting lattice distortion, etc [1, 7–18], with these assumption as a basis. It has however been found from x-ray and neutron diffraction (ND) measurements that many, if not all, of the alloys supposedly meeting the original definition of an HEA alloy are in reality multiphase with in most cases one main phase and one or several minor phases. From the literature and the authors' own experience [19–23], a more adequate definition of an HEA alloy would be that they are multicomponent alloys, presenting 'simple' diffraction patterns, e.g. consisting of one or several lattices of fcc or bcc or even hcp type with very close lattice parameters [22]. The alloys that are discussed below correspond to this definition. Many different techniques have been used to characterize the structure and microstructure of HEAs as well as their physical properties. With regard to magnetic properties, rather few studies have been reported, although it was earlier reported that HEAs may have and in some cases really have some interesting properties [2, 14, 24–28]. However, the understanding of the correlation between structure and physical property as well as between atomic and magnetic structures of these alloys is still unclear.

A great number of studies have been dealing with CoCrFeNi (below denoted CCFN) alloy which, even if it contains only four different elements, has to be considered as a basic HEA alloy. Recently, the CCFN alloy has been, in contradiction to earlier claims, shown to be at least dual-phase, consisting of two fcc structures with very close lattice parameters [22, 29] and its physical properties have been recently fully characterized [22, 23, 30]. The alloy has been found to be ferromagnetic at low temperature with a Curie temperature at around 120 K [26–33]. The physical properties including magnetic ones of a CCFN alloy at different relative element composition have also been studied by theoretical approaches [34, 35].

Out of the many CCFN-based alloys the CCFN-Pd alloy has been of rather limited interest. Its structure and some physical properties have been reported in [27, 28] and it was concluded to be single-phase and also to have some interesting magnetic properties. However, later experimental work showed undoubtedly that it is at least dual-phase with a structure clearly depending on the Pd content [20, 21]. The structural and magnetic properties of the CCFN-Pd_x alloys presented in this study have recently been fully characterized [22, 23, 30]. The diffraction investigations of CCFN-Pd_x alloys in as-produced condition have revealed that they contain at

least three phases with traces of a fourth one. The structural complexity is furthermore accentuated by another study [23] performed by microscopy techniques (EPMA, EDX, SEM) and atom probe tomography (APT) on the same alloys that have also shown the presence of at least three phases of different composition in CCFN-Pd_x alloys with x in the range $0 < x \leq 1.5$: (i) one main CCFN-rich phase, (ii) two minor phases, one FeCoCr-rich and one FeCrPd-rich phase and (iii) some traces of a FeCr-rich phase. The three first phases are of fcc type with very close lattice constant values.

The work presented below is aimed at understanding the impact of the structure (both atomic and magnetic) of the CCFN_yN alloys with different Fe content and of the CCFN-Pd_x alloys with different Pd content on both their electronic and magnetic behaviors. The structural and magnetic properties of these alloys were earlier investigated experimentally by x-ray and ND techniques [22] and magnetometry [30]. Two complementary approaches are used for electronic structure calculations, i.e. Korringa–Kohn–Rostoker method with the coherent potential approximation (KKR-CPA) for fully disordered structural models and within the *ab initio* framework of density functional theory (DFT) and the Vienna *ab initio* simulation package (VASP) for supercell models of HEA structures. The obtained results are also compared with experimental and calculated values of CCFN-Pd_x alloys reported in the literature [27, 28, 31]

2. Methods

2.1. Electronic structure calculations

Electronic structure calculations of disordered CCFN-Pd_x ($x = 0, 0.255, 0.545, 1.0, \text{ and } 1.5$) HEA alloys (fcc and bcc crystal structures) have been performed using the Green function charge- and spin-self-consistent KKR method with the use of the CPA to treat chemical disorder [36, 37]. In all considered systems, the equilibrium lattice constant (a_{\min}) has been determined from the minimum of the total energy (fitting to parabola) and the electronic structure and ground-state properties have been computed. The electronic structure and magnetic properties have also been calculated using the room temperature experimental value of lattice constants. The self-consistent crystal potential of *muffin-tin* form was constructed with the local density approximation (LDA) framework, using the Perdew–Wang formula for the exchange-correlation part. The KKR-CPA computations in disordered HEAs have been restricted to only the spherical part of the potential; to verify the validity of this hypothesis, the full-potential KKR method was also employed to compute the electronic structure of ordered fcc CCFN, where the full form of the crystal potential over the whole atomic Voronoi cells was applied, with l truncation on each atom up to $l_{\max} = 3$. For finally converged atomic charges below $10^{-3}e$ and potentials below 1 mRy ($Ry = 13.6\text{ eV}$), the total, site-decomposed and l -decomposed, density of states (DOS) were computed using the integration tetrahedron method in reciprocal space and 550 k -space points in the irreducible part of the Brillouin zone. Furthermore, the total magnetic moment (per Wigner–Seitz cell) and all atomic

magnetic moments (inside *muffin-tin* spheres) were calculated. The Fermi level, E_F , was precisely determined from the Lloyd method [38], which appears to be particularly important in systems close to the magnetic-nonmagnetic limit. In all figures presented here, E_F is located at zero and spin-polarized DOS curves are given in Ry^{-1} per spin direction. The core states were calculated fully relativistically, whereas the valence states were treated in a nonrelativistic approach.

The KKR and KKR-CPA electronic structure calculations correspond to the so-called ground-state properties of the investigated system, i.e. at $T = 0\text{K}$.

2.2. DFT calculations

DFT calculations with full relaxation of atoms were performed using the projector augmented wave (PAW) method implemented in the VASP [39, 40]. Exchange and correlation were treated in the Perdew–Burke–Ernzerhof generalized gradient approximation (PBE-GGA) [41]. PAW potentials were used without semi-core p electron contribution with 6, 8, 9, 10, and 10 electrons treated as valence for Cr, Fe, Co, Ni and Pd, respectively. Total energies were calculated using the Monkhorst–Pack mesh [42] of k -points in the Brillouin zone with k -mesh spacing of 0.2 \AA^{-1} , which corresponds to $6 \times 6 \times 6$ k -point mesh for a $2 \times 2 \times 2$ supercell of fcc cubic structure containing 32 atoms. The plane wave cut-off energy used in the calculations was 400 eV. The total energy convergence criterion was set to 10^{-5} eV/cell and the force components were relaxed to 10^{-3} eV \AA^{-1} .

The disordered CCFN and CCFN-Pd $_x$ alloys were investigated by an application of special quasi-random structures (SQSs) [43], which enabled us to model random configurations in a relatively small cell. SQSs for four-component fcc CCFN and five-component fcc CCFN-Pd $_x$ systems containing 32 and 108 atoms were generated using a method based on a Monte Carlo simulated annealing loop [44] as implemented in the alloy theoretic automated toolkit (ATAT) package [45]. The lattice sites of SQSs were occupied by constituent atoms in such a way that the average correlation functions closely reproduced that one of a completely random substitutional alloy. The occupation of atomic positions in the 32-atom SQSs of fcc $\text{Co}_8\text{Cr}_8\text{Fe}_8\text{Ni}_8$ (CCFN), $\text{Co}_7\text{Cr}_7\text{Fe}_7\text{Ni}_7\text{Pd}_4$ (CCFN-Pd $_{0.57}$), $\text{Co}_6\text{Cr}_7\text{Fe}_7\text{Ni}_6\text{Pd}_6$, $\text{Co}_5\text{Cr}_6\text{Fe}_6\text{Ni}_5\text{Pd}_{10}$, $\text{Co}_7\text{Cr}_7\text{Fe}_{11}\text{Ni}_7$ (CCF $_{1.52}\text{N}$), and $\text{Co}_4\text{Cr}_8\text{Fe}_8\text{Ni}_4\text{Pd}_8$ alloys as well as the 108-atom SQS and quasi-ordered structure of fcc $\text{Co}_{26}\text{Cr}_{26}\text{Fe}_{30}\text{Ni}_{26}$ (CCF $_{1.15}\text{N}$) alloy are presented in tables S1 and S2 in the supplementary material (stacks.iop.org/JPhysD/50/185002/mmedia).

The ordered CCFN configuration was created based on the four-atom structure of Fe_2CrNi intermetallic phase [46] by a replacement of one Fe atom with a Co atom. The quasi-ordered CCF $_{1.15}\text{N}$ structure was constructed based on the $3 \times 3 \times 3$ supercell of CCFN with 108 atoms by a replacement of a randomly chosen Cr, Co, and Ni atom by Fe atoms.

It is important to note that the VASP DFT calculations were using free energy, not only energy at $T = 0\text{K}$, because there is a smearing parameter of 0.1 eV in electron entropy calculations.

Table 1. Composition of the experimentally investigated alloys.

Name	Composition
CCFN	$\text{Co}_{25}\text{Cr}_{25}\text{Fe}_{25}\text{Ni}_{25}$
CCF $_{0.8}\text{N}$	$\text{Co}_{26.3}\text{Cr}_{26.3}\text{Fe}_{21.1}\text{Ni}_{26.3}$
CCF $_{1.2}\text{N}$	$\text{Co}_{23.8}\text{Cr}_{23.8}\text{Fe}_{28.6}\text{Ni}_{23.8}$
CCFN-Pd $_{0.5}$	$\text{Co}_{22.2}\text{Cr}_{22.2}\text{Fe}_{22.2}\text{Ni}_{22.2}\text{Pd}_{11.2}$
CCFN-Pd $_{0.8}$	$\text{Co}_{20.8}\text{Cr}_{20.8}\text{Fe}_{20.8}\text{Ni}_{20.8}\text{Pd}_{16.8}$
CCFN-Pd $_{1.0}$	$\text{Co}_{20}\text{Cr}_{20}\text{Fe}_{20}\text{Ni}_{20}\text{Pd}_{20}$
CCFN-Pd $_{1.2}$	$\text{Co}_{19.2}\text{Cr}_{19.2}\text{Fe}_{19.2}\text{Ni}_{19.2}\text{Pd}_{23.2}$
CCFN-Pd $_{1.5}$	$\text{Co}_{18.2}\text{Cr}_{18.2}\text{Fe}_{18.2}\text{Ni}_{18.2}\text{Pd}_{27.2}$

2.3. Experimental procedures

CoCrFeNi-Pd_x ($x = 0.0, 0.5, 0.8, 1.0, 1.2, 1.5$) as well as $\text{CoCrFe}_{0.8}\text{Ni}$ and $\text{CoCrFe}_{1.2}\text{Ni}$ HEAs (in the following denoted CCFN-Pd $_x$, CCF $_{0.8}\text{N}$, and CCF $_{1.2}\text{N}$ respectively) were prepared as described elsewhere [22, 23]. The nominal composition of the investigated alloys is given in table 1.

In order to determine the structure of the alloys at the atomic level, three different experimental diffraction techniques were used and extensively reported elsewhere [22]: standard x-ray diffraction (XRD), high-energy x-ray diffraction (HEXRD) and ND. When comparing the structures obtained from different diffraction measurements it is important to note that the penetration depth of the standard laboratory x-rays in a CCFN alloy is of the order of $1 \mu\text{m}$ and thus as the measurements are necessarily performed in reflection geometry they give structure information only for a surface layer. On the other hand ND and HEXRD measurements were performed in transmission geometry, thus giving information on the bulk structure of the alloys.

Macroscopic magnetic properties of the alloys were investigated with a superconducting quantum interference device (SQUID) at temperatures from 5–400 K and reported elsewhere [30]. The evolution of the magnetization as a function of applied magnetic field was measured at 5 and 300 K and the thermal variation of the magnetization of the alloys was measured under an applied magnetic field of 100 Oe [30].

Although the experimental data have already been reported separately, they are here presented in perspective and in comparison with theoretical calculations. The combination of electronic, structural, and magnetic properties is a key issue to understand the complexity of HEAs.

3. Results

3.1. Structure

For reference, the lattice constants of the produced alloys determined by diffraction measurements using three different kinds of radiation, high-energy x-rays, standard x-rays, and neutrons are given in table 2 [22]. All Pd-containing alloys have been found to consist of at least three different phases, all being of fcc type. Because of the different resolution of the three diffraction techniques, only two phases could be observed by ND and standard XRD. The lattice constants for all phases increase continuously with Pd content, which indicates that Pd atoms have been incorporated into the CoCrFeNi

Table 2. Determined fcc lattice constants, in Å, of investigated CCF_yN ($y = 0.8$ and 1.2) and CCFN-Pd_x ($x = 0, 0.5, 0.8, 1.0, 1.2, 1.5$) alloys in as-cast conditions. Phase 1, phase 2, and phase 3 correspond to two or three intensity components identified by decomposition of the measured diffraction peaks [22].

Alloy	High-energy x-rays (HEXRD)			Standard x-rays (XRD)		Neutrons (ND)	
	Phase 1	Phase 2	Phase 3	Phase 1	Phase 2	Phase 1	Phase 2
$\text{CCF}_{1.0}\text{N}$	—	—	—	3.573(2)	—	3.570(3)	—
$\text{CCF}_{0.8}\text{N}$	3.5721(1)	3.5733(3)	—	3.575(3)	—	3.580(3)	—
$\text{CCF}_{1.2}\text{N}$	3.5749(2)	3.5770(5)	—	3.572(3)	—	3.575(3)	—
$\text{CCFN-Pd}_{0.5}$	3.6201(3)	3.6327(6)	3.6437(8)	3.631(3)	3.643(5)	—	—
$\text{CCFN-Pd}_{0.8}$	—	—	—	—	—	3.634(2)	3.656(3)
$\text{CCFN-Pd}_{1.0}$	3.6595(3)	3.6752(7)	3.6871(6)	3.662(3)	3.678(5)	3.656(2)	3.673(3)
$\text{CCFN-Pd}_{1.2}$	—	—	—	—	—	3.668(3)	3.686(3)
$\text{CCFN-Pd}_{1.5}$	3.699(1)	3.705(1)	3.710(1)	3.705(3)	3.721(5)	—	—

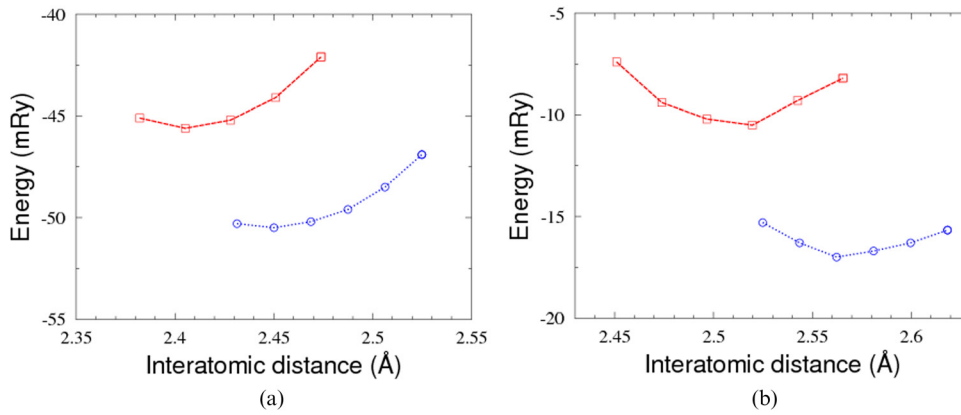


Figure 1. KKR-CPA total energy versus interatomic distance in fcc (low curve, blue circles) and bcc (top curve, red squares) structures of CCFN (a) and $\text{CCFN-Pd}_{1.0}$ (b) HEAs.

lattice. The relative amounts of the different phases were found to depend on Pd concentration. It can also be seen that a change of the amount of Fe in the base CCFN alloy only has a very small effect on the lattice constant.

Furthermore, another study [23] on the same samples by microscopy techniques (EPMA, EDX, SEM) and APT have revealed the presence of four phases in the CCFN-Pd_x samples: (i) one CCFN-rich phase, the main one detected by diffraction [22], (ii) plus two second phases, one FeCoCr-rich, maybe corresponding to one observed in some other CCFN-base alloys (e.g. [47]) and one FeCrPd-rich phase. In addition, some traces of an FeCr-rich phase have also been observed. The three first phases are of fcc type with very close lattice constant values (see table 2 [22]). All fcc phases do not seem to be distorted but have some degree of occupational disorder, although not to the extent that they can be characterized as perfect solid solutions.

As the HEA alloys usually exhibit bcc/fcc phase preference or their coexistence, these two types of structures were accounted for in the KKR-CPA computations (assuming random distribution of all atoms on the same crystallographic site) of CCFN-Pd_x by varying the lattice parameters and Pd content. In order to conveniently compare results obtained for bcc and fcc phases, the total energy is plotted as a function of interatomic distance (d), which is comparable in both structures. Figures 1(a) and (b) show that the fcc structure is

Table 3. The lattice parameter, in Å, deduced from the KKR-CPA total energy minimum, in fcc CCF_yN and CCFN-Pd_x alloys.

fcc structure	Lattice constant (Å)
CCFN disordered	3.462
CCFN^a	3.496
CCFN^b	3.504
CCFN ordered	3.572
$\text{CCF}_{0.8}\text{N}$ disordered	3.460
$\text{CCF}_{1.2}\text{N}$ disordered	3.465
$\text{CCFN-Pd}_{0.255}$	3.531
$\text{CCFN-Pd}_{0.545}$	3.579
$\text{CCFN-Pd}_{1.0}$	3.636
$\text{CCFN-Pd}_{1.5}$	3.695

^{a, b} Partially disordered models (see text).

much more favorable than the bcc one in view of total energy analysis of both CCFN and $\text{CCFN-Pd}_{1.0}$. The preference of fcc structure is clearly seen from the much lower ground-state energy. This preference appears in the wide range of interatomic distances around the equilibrium lattice parameter and the curves computed for bcc and fcc do not intersect. Similar structural behavior was found for other Pd content. Other results obtained using the combination of DFT, frozen potential, and rigid band approximations also show that the fcc

Table 4. Enthalpy of formation per atom (in eV), H_{form} , volume per atom (in \AA^3), V , average magnetic moment per atom (in μ_B), m_{atom} , and average magnetic moment of each constituents, m_i ($i = \text{Co, Cr, Fe, Ni, Pd}$), calculated for fully relaxed disordered and ordered fcc $\text{CoCrFe}_y\text{Ni-Pd}_x$ structures. ‘Q-ordered’ stands for quasi-ordered.

fcc $\text{CoCrFe}_y\text{Ni-Pd}_x$	y	x	H_{form}	V	m_{atom}	m_{Co}	m_{Cr}	m_{Fe}	m_{Ni}	m_{Pd}
CCFN ordered	1.0	0	-0.017	11.21	0.22	0.88	-2.38	2.25	0.16	
CCFN SQS	1.0	0	0.087	11.13	0.64	1.07	-0.93	2.16	0.26	
CCF _{1.52} N SQS	1.52	0	0.081	11.13	0.67	0.93	-1.34	2.09	0.22	
CCF _{1.15} N Q-ordered	1.15	0	-0.013	11.21	0.32	0.93	-2.34	2.25	0.18	
CCF _{1.15} N SQS	1.15	0	0.082	11.13	0.67	1.09	-0.94	2.06	0.26	
CCFN-Pd _{0.57} SQS	1	0.57	0.089	11.96	0.55	1.38	-1.56	2.46	0.27	0.09
CCFN-Pd _{1.0} ordered	1	1.0	0.103	12.15	0.95	1.63	0.06	2.63	0.34	0.12
Co ₆ Cr ₇ Fe ₇ Ni ₆ Pd ₆ SQS	1	~0.92	0.115	12.21	0.53	1.34	-1.45	2.47	0.28	0.09
Co ₅ Cr ₆ Fe ₆ Ni ₅ Pd ₁₀ SQS	1	~1.82	0.075	12.85	0.41	1.50	-2.03	2.62	0.32	0.10
Co ₄ Cr ₈ Fe ₈ Ni ₄ Pd ₈ SQS			0.101	12.68	0.61	1.41	-1.04	2.53	0.34	0.13

Table 5. Average lattice parameter, a_{av} , lattice parameters in three directions, a_1 , a_2 , and a_3 , as well as their deviations from the average lattice parameter, $a_1 - a_{\text{av}}$, $a_2 - a_{\text{av}}$, $a_3 - a_{\text{av}}$, (all values in \AA) calculated for fully relaxed disordered and ordered fcc $\text{CoCrFe}_y\text{Ni-Pd}_x$ structures. ‘Q-ordered’ stands for quasi-ordered.

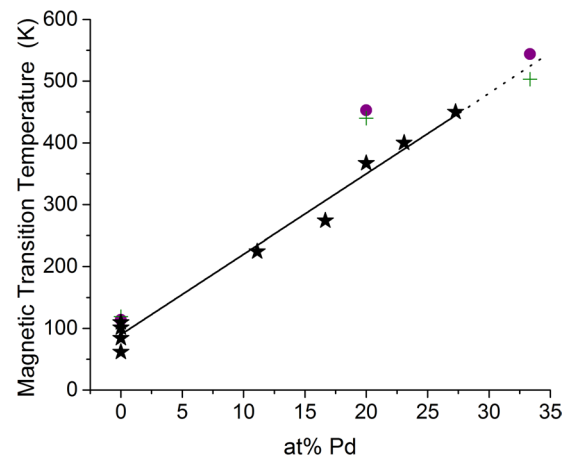
fcc $\text{CoCrFe}_y\text{Ni-Pd}_x$	y	x	a_{av}	a_1	a_2	a_3	$a_1 - a_{\text{av}}$	$a_2 - a_{\text{av}}$	$a_3 - a_{\text{av}}$
CCFN ordered	1.0	0	3.553	3.532	3.563	3.562	-0.021	0.010	0.009
CCFN SQS	1.0	0	3.544	3.524	3.552	3.557	-0.020	0.008	0.013
CCF _{1.52} N SQS	1.52	0	3.544	3.503	3.551	3.578	-0.041	0.007	0.034
CCF _{1.15} N Q-ordered	1.15	0	3.553	3.557	3.535	3.566	0.004	-0.018	0.013
CCF _{1.15} N SQS	1.15	0	3.544	3.537	3.539	3.557	-0.007	-0.005	0.013
CCFN-Pd _{0.57} SQS	1	0.57	3.630	3.600	3.622	3.668	-0.030	-0.008	0.038
CCFN-Pd _{1.0} ordered	1	1.0	3.649	3.636	3.636	3.675	-0.013	-0.013	0.026
Co ₆ Cr ₇ Fe ₇ Ni ₆ Pd ₆ SQS	1	~0.92	3.655	3.649	3.650	3.667	-0.006	-0.005	0.012
Co ₅ Cr ₆ Fe ₆ Ni ₅ Pd ₁₀ SQS	1	~1.82	3.718	3.693	3.725	3.736	-0.025	0.007	0.018
Co ₄ Cr ₈ Fe ₈ Ni ₄ Pd ₈ SQS			3.702	3.693	3.686	3.727	-0.009	-0.016	0.025

phase of CCFN-Pd_x alloys is more stable than bcc phase for the same concentration of Pd [35].

In the case of fcc CCFN-Pd_x, the KKR-CPA total energy calculations assuming fully disordered model (random distribution of all atoms) allowed us to determine the evolution of the lattice parameter with Pd content. As expected from the sizes of the atom radii, palladium substituted into the CCFN matrix expands the unit cell, which is clearly seen in table 3.

The DFT enthalpies of formation, defined as the energy of a structure with respect to the energy of bcc Cr, bcc Fe, hcp Co, fcc Ni, and fcc Pd, are given in table 4. It is worth noting that negative enthalpy of formation has been predicted for ordered CCFN and quasi-ordered CCF_{1.15}N. The enthalpies of formation of disordered alloys represented by SQSs have been found to be positive. The phase stability and structural analysis of CCF_yN and CCFN-Pd_x alloys and the effect of short-range order (SRO) will be further addressed in section 4.

Tables 4 and 5 present the DFT calculated volumes of fully relaxed structures and average lattice parameters, a_{av} , obtained from these volumes, for all considered CCF_yN and CCFN-Pd_x alloys. For the SQS CCFN-Pd_x configurations, the DFT calculations predict that the average lattice parameters increase as a function of Pd concentration, which is consistent with the fact that Pd atom has the largest size of all considered elements. The detailed comparison with the experimental data will be given below.

**Figure 2.** Magnetic transition temperature, T_{trans} , as a function of the at.% Pd for the experimental values determined from SQUID $M(T)$ data on CCF_yN-Pd_x alloys at 100 Oe (★ black) [30] and from the literature by Lucas (+green) [27] and K ormann (● purple) [31].

3.2. Magnetic properties

The magnetic transition temperatures T_{trans} were calculated from the derivative of the temperature variation of the magnetization at 100 Oe between 5 and 400 K [30]. The variation of

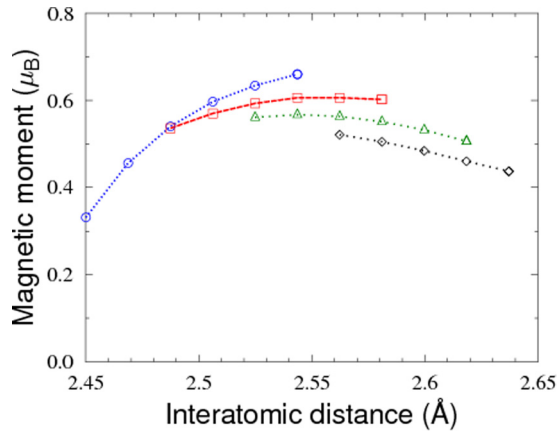


Figure 3. The variation of the total magnetic moments per site as a function of lattice constant in fcc CCFN-Pd_x for $x = 0$ (blue circles), 0.5 (red squares), 1.0 (green triangles), and 1.5 (black lozenges) as computed with the KKR-CPA method.

the transition temperatures as a function of the Pd content is presented in figure 2.

From figure 2, it can be seen that there is an almost linear relationship between T_{trans} and Pd content of an alloy at small Pd content, which is in good agreement with earlier experimental as well as theoretically calculated (DFT + magnetic mean-field model) T_{trans} [31].

The average magnetic moment per atom was determined by the value at saturation of the variation of the magnetization as a function of applied magnetic field at 5 K. The data are presented below in comparison with the calculations. Extensive study of the magnetic properties of the CCFN-Pd_x alloys is presented elsewhere [30].

The variation of total magnetic moments (per site) and local magnetic moments (per atom) were calculated by the KKR-CPA method as a function of the lattice constant in the fcc phase of CCFN-Pd. The results are presented in figures 3 and 4, respectively. One can observe that magnetic (actually ferrimagnetic) properties of these alloys are dominated by large magnetic moments appearing on Fe and Co atoms as well as antiparallel coupled moment on Cr atom, due to strong spin polarization of the respective DOS (figure 5). These three magnetic moments significantly vary with lattice constant, but this variation tends to be smaller with increasing Pd content. Conversely, Ni atoms in CCFN-Pd keep much lower magnetic moment (c.a. $0.4 \mu_B$), which is found to be almost insensitive to change of lattice parameter. The contribution of Pd atoms to the magnetism of CCFN-Pd can be neglected (not presented). On the whole, the variation of total magnetic moment versus lattice parameter in these alloys is governed by a subtle balance between individual variations of ferromagnetically coupled moments on Fe, Co, and Ni and an antiferromagnetically aligned one on Cr. The KKR-CPA calculations show that in spite of the fact that all magnetic moments increase (in absolute value) with increasing Pd content, the magnetic moment of Cr decreases more rapidly than those of Fe, and Co increases (figures 4(a)–(c)). As a result, the computed total magnetic moment apparently increases at lower Pd content ($0.50 \mu_B$ for $x = 0.5$ against only $0.28 \mu_B$ for $x = 0$), but it

tends to slightly decrease at higher Pd content ($0.56 \mu_B$ for $x = 1$ versus $0.47 \mu_B$ for $x = 1.5$). The direct comparison of the obtained theoretical results with the experimental values of magnetization is not simple. This is because all the above-mentioned samples (whatever the Pd content) contain two or more fcc phases with slightly different lattice parameters. The KKR-CPA calculations clearly indicate the important effect of interatomic distance on computed magnetic moments, dependent both on type of atoms and alloy composition. Consequently, it seems more reasonable to compare general trends than particular values of magnetic moments, which is however tentatively done in table 6.

It is worth noting the overall increase of magnetic moments on all constituent atoms with Pd content increase (causing the unit cell expansion) indicates systematic enhancement of magnetic interactions. This theoretical result qualitatively corroborates with the observed increase of magnetic transition temperature in CCFN-Pd_x with x increase (figure 2).

The average magnetic moment per atom, m_{atom} , assuming random distribution of all atoms in the fcc structure have also been derived from KKR-CPA in CCF_yN ($y = 0.8, 1.0$ and 1.2) at minimal lattice constant. In this case, the lattice parameter is found to remain almost constant with the variation of Fe content, which well corresponds to experimental data (table 3). Conversely, the average magnetic moment grows in CCF_yN from $0.24 \mu_B$ for $y = 0.8$ to $0.30 \mu_B$ for $y = 1.2$, mostly due to the effect of the increased concentration of Fe atoms, which keeps the largest magnetic moment among constituent atoms.

4. Discussion

4.1. Structure

For comparison, some calculations and experimental results from the literature have been inserted in figures 6 and 7, representing the variation of lattice constant as a function of Fe and Pd content. The average magnetic moment as well as lattice constants have been reported for some CCFN-Pd alloys in [27]. However, the alloys were prepared by arc melting under an argon atmosphere and the as-cast buttons were cold rolled to thicknesses of 100–250 μm . The structure was determined by standard XRD at ambient temperature and it was concluded by the authors that the alloys had a single phase fcc structure and formed a solid solution.

The calculated and experimentally obtained lattice constants are presented in figures 6(a) and (b).

As shown above (table 3), the KKR-CPA results show that the most energetically favorable structure for all alloys is fcc. This is in accordance with the diffraction results for the main phase (phase 1 in table 2) [22]. Thus, only results regarding fcc structures are shown in figures 6 and 7. It can be deduced that there is also a general agreement between the diffraction results for the main phase (CoCrFeNi-rich [23]) in both sets of calculations. However, the two additional fcc phases found to be present in diffraction measurements on the CCFN-Pd as-cast alloys are not reproduced in any of the calculations. Moreover, with regard to the CCFN alloy the experimental values are satisfactorily reproduced by KKR-CPA ordered

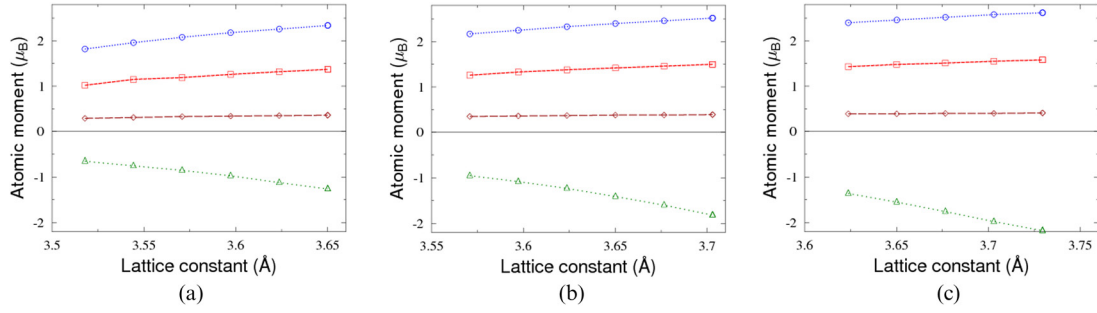


Figure 4. (a)–(c) The variation of local magnetic moments per atom as a function of the lattice constant in fcc phase of CCFN-Pd_{0.5} (a), CCFN-Pd_{1.0} (b), and CCFN-Pd_{1.5} (c). Fe (blue circles), Co (red squares), Ni (brown lozenges), Cr (green triangles).

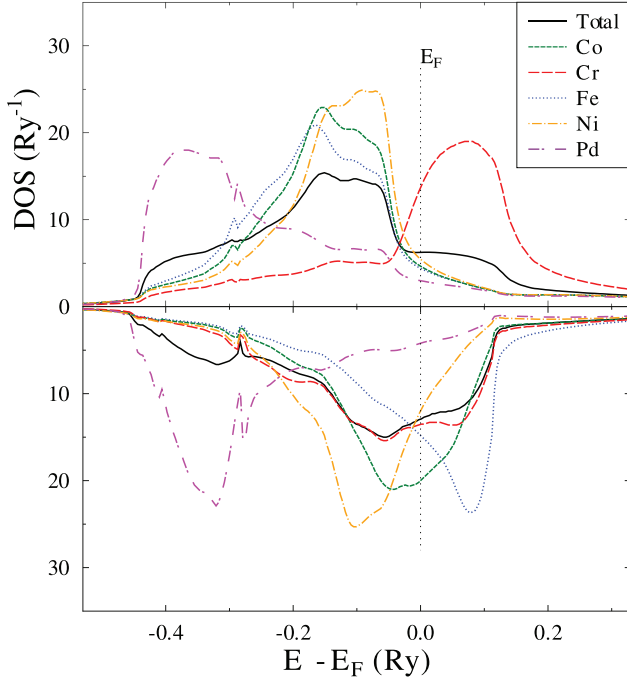


Figure 5. KKR-CPA DOS in the equimolar CoCrFeNiPd HEA. Total (black, solid) and site-decomposed contributions, i.e. Co (green, long-dashed), Cr (red, short-dashed), Fe (blue, dotted), Ni (orange, dot-dashed), and Pd (magenta, dot-dashed) are plotted. The Fermi energy (E_F) is shifted to zero.

calculations (figure 6(a)) and to a lesser extent by the VASP ordered models.

It is important to note also that the VASP DFT calculated average lattice parameters of fully relaxed structures for all CCF_yN and CCFN-Pd_x alloys also predict clearly that the HEAs are only fcc-like configurations. The lattice constants are well reproduced for CCFN-Pd_x alloys (figure 6(b)) by the calculated average value, but not for CCFN (figure 6(a)). However, the three calculated different lattice parameters depending on the crystallographic direction, (see table 5) do not reproduce the lattice constant values, nor the variation, of the three phases clearly identified in the diffraction measurements (figures 7(a) and (b)). Thus, the difference in lattice constants identified by diffraction [22] is due to the presence of different fcc phases as observed in [23], not by distortions in different crystallographic directions as can be clearly seen by comparing figures 6(b) and 7(b). The present DFT studies

Table 6. Average magnetic moment per atom, m_{atom} , derived from KKR-CPA at minimal lattice constant.

fcc disordered structure	m_{atom} (μ_B)
CCF _{0.8} N	0.24
CCFN	0.28
CCFN ^a	0.46
CCFN ^b	0.42
CCFN ordered	0.24
CCF _{1.2} N	0.30
CCFN-Pd _{0.255}	0.55
CCFN-Pd _{0.545}	0.60
CCFN-Pd _{1.0}	0.56
CCFN-Pd _{1.5}	0.47

^{a, b} Partially disordered models.

show clearly the important role played by chemical short-range order (CSRO) parameters in the structural analysis of multi-component HEAs, which is very consistent with previous studies of magnetic ternary Fe–Cr–Ni alloys [46] and experimental observation [48].

It can furthermore be seen in figure 6(a) that the KKR-CPA lattice constants tend to underestimate the experimental data, which is in line with the well-known LDA limits. The most severe discrepancy was found for the CCFN alloy, disordered, where the lattice parameter of only 3.462 Å was computed compared to the experimentally measured values that lie in the range from 3.57–3.58 Å [20]. This circumstance prompted us to shed light on the CCFN case in a different way. It is worth noting that the fcc CCFN alloy, due to four crystallographic sites A: (0, 0, 0), B: (1/2, 1/2, 0), C: (1/2, 0, 1/2), and D: (0, 1/2, 1/2) and four atoms (Co, Cr, Fe, and Ni) in the unit cell, may exhibit propensity to form more ordered-like structures than the fully disordered one. To investigate the increasing effect of disorder, or to put it differently, a tendency to form more ‘ordered’ structures in the CCFN sample, few models were accounted for by the KKR-CPA calculations. The crystal structure models with gradually increasing chemical disorder means that the unit cell may contain different arrangements of atoms, but in principle all these models must be between the limiting cases: (i) fully ordered model when only one atom occupies one crystallographic site in a simple cubic unit cell, i.e. A(Co):B(Cr):C(Fe):D(Ni) as well as all possible permutations and (ii) fully disordered model when all four atoms are

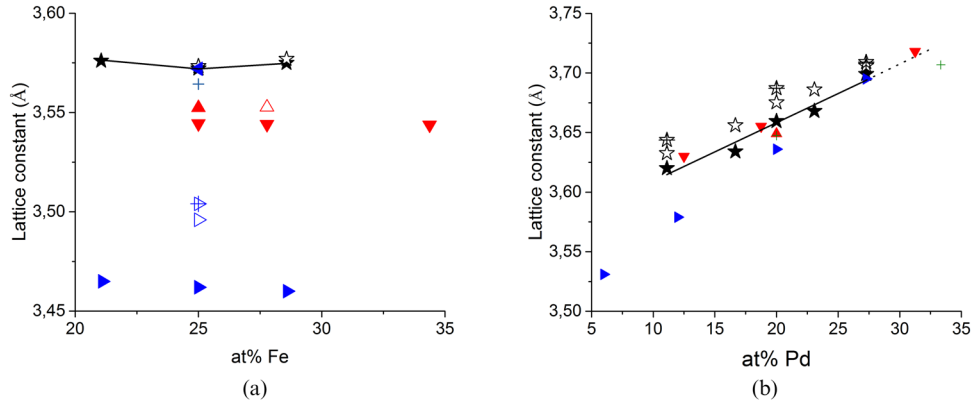


Figure 6. (a) and (b) Comparison between experimental [22] and calculated values of the lattice constant of $\text{CCF}_y\text{N-Pd}_x$ alloys as a function of (a) the at%Fe and (b) the at%Pd for (black phase 1 \star , phase 2 \star , and phase 3 \star) experimental diffraction data with black solid line for the first phase in table 2. (Blue \blacktriangleright , \triangleright , and \oplus) KKR-CPA disordered and partially disordered configurations listed in table 3, (blue \blacktriangleleft) KKR-CPA ordered configuration listed in table 3, (red \blacktriangledown , \blacktriangle , and \triangle) average VASP SQS, ordered, and quasi-ordered configurations listed in table 5, and (green +) Lucas *et al* [27].

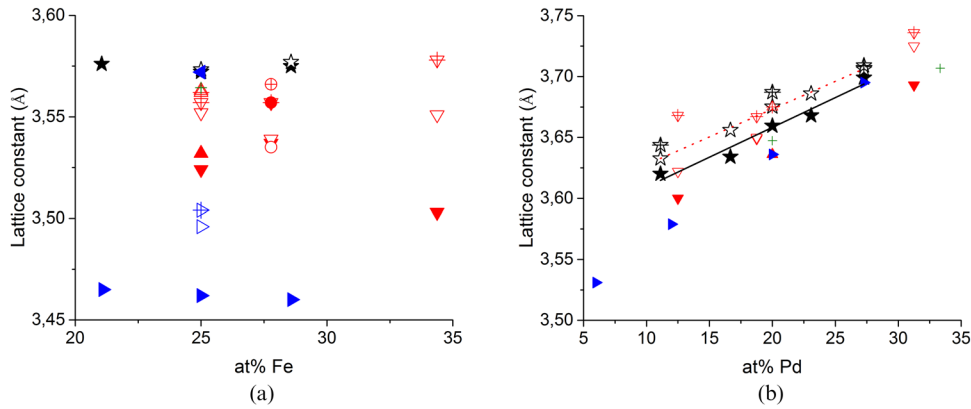


Figure 7. (a) and (b) Comparison between experimental [22] and calculated values of the lattice constant of $\text{CCF}_y\text{N-Pd}_x$ alloys as a function of (a) the at%Fe and (b) the at%Pd for (black \star , \star , and \star) experimental diffraction data, with black solid and red dotted lines for the two main phases in table 2. (blue \blacktriangleright , \triangleright , and \oplus) KKR-CPA disordered configurations listed in table 3, (blue \blacktriangleleft) KKR-CPA ordered configuration listed in table 3, (red \blacktriangledown , ∇ , ∇ , \blacktriangledown , \blacktriangle , \triangle , \oplus , and red \bullet , \circ , \oplus) three lattice parameters of VASP disordered, ordered, and quasi-ordered configurations respectively, (a_1 , a_2 , and a_3 listed in table 5), and (green +) Lucas *et al* [27].

randomly distributed on all four sites (i.e. 25%Co + 25%Cr + 25%Fe + 25%Ni on each of A–D sites), which actually represents fully disordered fcc structure. However, one can admit that occupancies of each of the A–D sites differ from the random case, i.e.

$$\text{A}(70\% \text{Co} + 10\% \text{Cr} + 10\% \text{Fe} + 10\% \text{Ni}),$$

$$\text{B}(10\% \text{Co} + 70\% \text{Cr} + 10\% \text{Fe} + 10\% \text{Ni}),$$

$$\text{C}(10\% \text{Co} + 10\% \text{Cr} + 70\% \text{Fe} + 10\% \text{Ni}),$$

$$\text{D}(10\% \text{Co} + 10\% \text{Cr} + 10\% \text{Fe} + 70\% \text{Ni})$$

to allow for maintaining the stoichiometric alloy. Besides, to account for KKR-CPA computations, any tendencies to spatially separate selected atoms of a system, due to specific electronic or magnetic interactions, the A–D sites can be occupied by three atoms, e.g. A(Co/Cr/Fe), B(Cr/Fe/Ni), C(Fe/Ni/Co), D(Ni/Co/Cr) or only by two atoms, e.g. A(Co/Cr), B(Cr/Fe), C(Fe/Ni), D(Ni/Co) and other possible configurations. Hence, to some extent, performing such KKR-CPA calculations, i.e. accounting for twofold, threefold, and finally fourfold atomic

disorder on crystallographic sites, the effect of increasing disorder can be investigated in a systematic way. Interestingly, it was found that simulating the partial disorder of atoms in the CCFN alloys tends to shift the minimum lattice parameter into a larger value and in the aforementioned model with the occupancies, namely 70% of the dominant atom and 10% for the other three atoms, it yields the value of 3.496 Å, which decreases the discrepancy with the experimental value to about 2%. Further increase of atom ‘ordering’ in the unit cell, namely computing the threefold disorder (three atoms on one crystallographic site with different occupancies, e.g. 80% of the dominant atom and 10% for the other two atoms) resulted in the value of 3.504 Å in the CCFN alloy. From figures 6(a) and (b), the fully ordered structure is the best-fitting configuration for CCF_yN , whereas the disordered ones reproduce better the CCFN-Pd_x alloys.

4.2. Magnetic properties

Importantly, one should also note a correlation between CSRO and magnetic properties as has been shown for the case of fcc Fe–Ni alloys [49] and most recently by experimental evidence

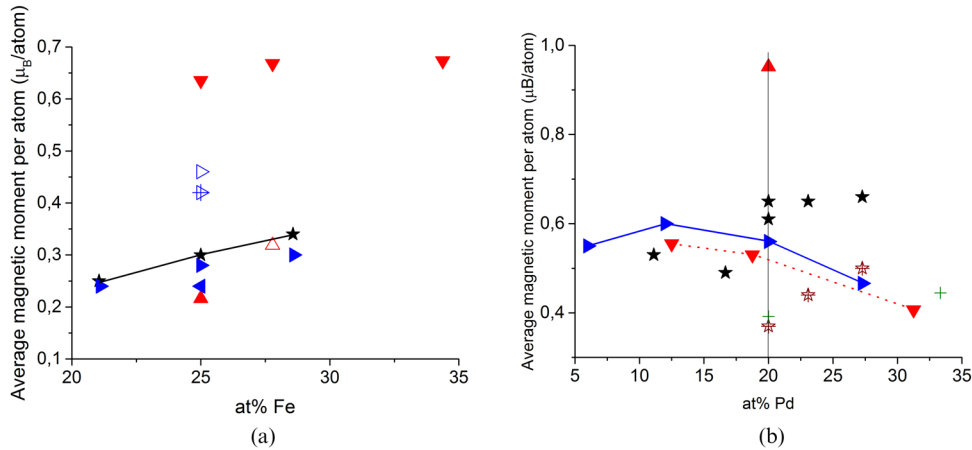


Figure 8. (a) and (b) Comparison of experimental [30] and calculated values of the average magnetic moment per atom, m_{atom} , of $\text{CCF}_y\text{N-Pd}_x$ alloys as a function of (a) the at%Fe and (b) the at%Pd: (black \star and black solid line, brown \star) experimental measurements at 5 and 300 K, (blue \blacktriangleright and solid line, \triangleright and \blacktriangleleft) KKR-CPA disordered configurations listed in table 6, (blue \blacktriangleleft) KKR-CPA ordered configuration listed in table 6, (red \blacktriangledown dotted line, \blacktriangle , and \triangle) VASP disordered, ordered, and quasi-ordered configurations, respectively, listed in table 4 and (green $+$) Lucas *et al* [27]. The vertical bar represents the equimolar composition.

[32]. On the whole, the lattice parameter of the CCFN system was found to be very sensitive to any type of local atom arrangements. This behavior also has a significant effect on magnetic interactions and calculated magnetic moments on atoms.

In CCFN, better agreement with the experimental lattice parameter is obtained when including partial disorder (figure 8(a)), not the fully disordered model (random distributions of atoms on crystallographic sites) in KKR-CPA calculations. This is also the case, to some extent, with VASP-DFT. The VASP-DFT calculations for the fully relaxed configurations in CCF_yN alloys show that the average lattice parameters for ordered and quasi-ordered structures as well as the average magnetic moment dependence as a function of Fe content are in a better agreement with the measured experimental data than those obtained from the disordered SQS configurations (figures 6(a) and 8(a)). It is interesting to note that the average magnitude of magnetic moment of Cr in the ordered fcc CCFN structure (see table 4) is found to be $-2.38 \mu_B$, which is more than two-and-a-half times larger than that of disordered structure. Consequently, since the magnetic moments of the other elements do not change significantly as a function of chemical ordering, the average magnetic moment of ordered fcc CCFN phase equals $0.22 \mu_B$, which is almost three times smaller than that of fcc CCFN SQS. This is in close agreement with both theoretical and experimental observations reported in [32]. Importantly, the DFT calculations presented in this study predicted the negative enthalpies of formation for the ordered and quasi-ordered CCF_yN alloys and therefore provided *ab initio* evidence of these stable configurations. New experimental works are needed for validating this new prediction, although the previous experimental studies indicated that CSRO and magnetic ordering play important roles in the structural stability of CCFN HEAs [32, 48].

Since the ordered CCFN structure is the most stable of all considered structures, see table 4 and section 3.1, the CCFN alloy might prefer to form ordered or partially SRO phases.

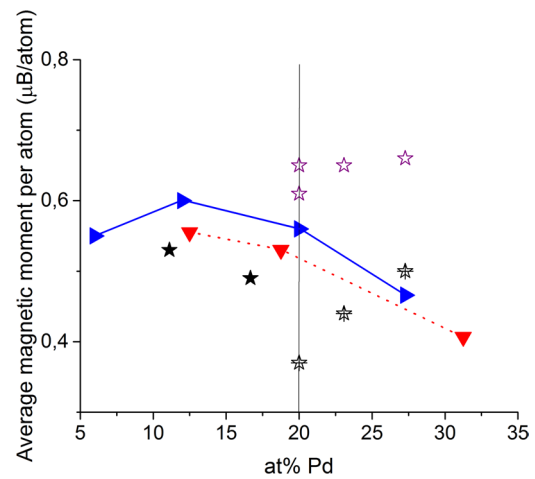


Figure 9. Comparison between experimental [30] and calculated values of the average magnetic moment per atom, m_{atom} , of $\text{CCF}_y\text{N-Pd}_x$ alloys as a function of the at%Pd: (black \star) HTM samples measured at 5 K, (black \star) HTM samples measured at 300 K, (purple \star) LTM samples measured at 5 K, (blue \blacktriangleright , solid line) KKR-CPA disordered configurations listed in table 6, (red \blacktriangledown dotted line) VASP disordered configurations listed in table 4. The vertical bar represents the equimolar composition.

The change in concentration of constituents causes the deviation from the stoichiometric concentration of CCFN and the decrease of SRO. As a consequence, the average magnetic moment of $\text{CCF}_{1.15}\text{N}$, $\text{CCF}_{1.57}\text{N}$, and all CCFN- Pd_x structures is larger than that of ordered CCFN (figures 8(a) and (b)). For example, the average magnetic moment of quasi-ordered $\text{CCF}_{1.15}\text{N}$ phase equal to $0.32 \mu_B$ is almost 50% larger than that of ordered CCFN. It is important to note that the former value is in very good agreement with the experimental value (figure 7(a)). The same trend is observed with KKR-CPA calculations (figure 8(a)).

Accordingly, the lattice constants and the average magnetic moment per atom are both well reproduced by ordered calculations or by including partial disorder for CCF_yN alloys (figures 6(a) and 8(a)).

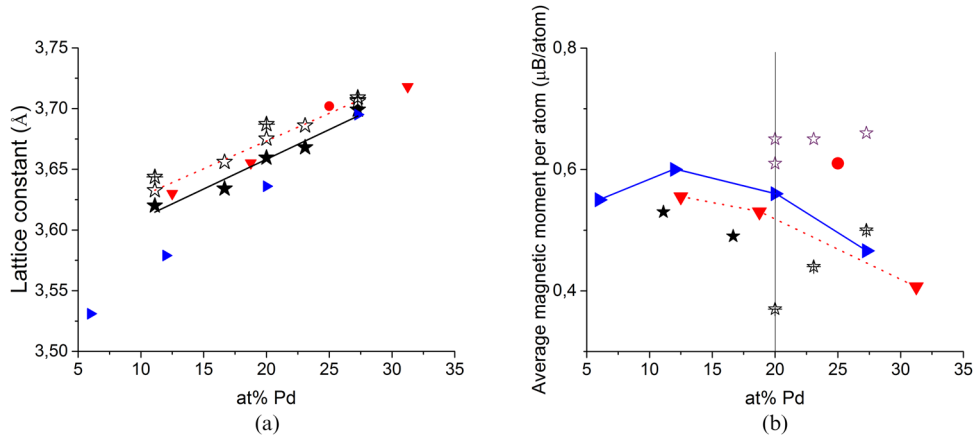


Figure 10. (a) and (b) Comparison between experimental [22, 30] and calculated values of the lattice constant (a) and average magnetic moment per atom (b) of CCFN-Pd_x alloys as a function of at%Pd for (black phase 1 ★, phase 2 ☆, and phase 3 ☆) experimental diffraction data, with a solid and dotted line for the two main phases in table 2. (Blue ► and solid line) KKR-CPA disordered configurations listed in table 3, (red ▼ and dotted line) VASP disordered configurations, (red ●) VASP Co₄Cr₈Fe₈Ni₄Pd₈ SQS listed in table 4. The vertical bar represents the equimolar composition.

In contrast, for CCFN-Pd_x alloys, when comparing the calculated and experimental values of the average magnetic moment per atom (figure 8(b)), the experiments are quite reproduced up to the equimolar composition, but not above by disordered models. Although the lattice constants are well predicted by both ordered and disordered configurations, the average magnetic moment values for the ordered ones are well above the experimental values (figure 8(b)). From the hysteresis loops measured at 5 K [30], CCFN-Pd_x alloys exhibit an extremely soft ferromagnetic behavior, with a saturation magnetization strongly dependent on the Pd content. However, the reported magnetic characteristics by [27] were measured with a vibrating sample magnetometer from room temperature to 1000 °C and upon cooling under an applied field of 0.05 T. The saturation magnetization was acquired before and after the high-temperature moment measurements at an applied field of 2 T.

The average magnetic moments of disordered fcc SQSs obtained using DFT simulations with full ionic relaxation (table 4) predict that the average magnetic moment of disordered fcc, SQSs, decreases when the concentration of Pd increases with a maximum value of 0.64 μ_B for fcc CCFN SQSs and a minimum value of 0.41 μ_B for fcc Co₅Cr₆Fe₆Ni₅Pd₁₀ SQSs up to the equimolar composition. The same trend is shown with the KKR-CPA calculations. The experimental values above the equimolar composition at 5 K are not satisfactorily reproduced by any of the calculations.

One can also observe that both calculations are well in line with the experimental values at 300 K and the values from [27] also performed above room temperature.

At this point, the following should be noted:

- (1) According to figure 2, the alloys with Pd composition above equimolar have a magnetic transition above room temperature. This means that at room temperature, they still have the low-temperature magnetic structure.
- (2) According to figure 2, the alloys with composition below equimolar have a magnetic transition below room temperature. Thus, at room temperature, they have the high-temperature structure already.

- (3) When the measurement of the average magnetic moment per atom at 5 K is performed, the sample is first rapidly cooled to 5 K. Afterwards, the recording of the magnetization as a function of applied field starts at constant temperature, 5 K.
- (4) When the measurement of the average magnetic moment per atom at 300 K is performed, the sample is first rapidly heated to at least 300 K. Afterwards, the recording of the magnetization as a function of applied field starts at constant temperature, 300 K.

Consequently, one can divide the results of the magnetization in two groups:

- (1) HTM: samples having the high-temperature magnetic structure, i.e. the ones that have a magnetic transition below room temperature and are measured at 5 K. One can suppose that the structure is preserved by the rapid cooling to 5 K from room temperature. In this category are also the samples that have a magnetic transition above room temperature and measured at 300 K.
- (2) LTM: samples having the low-temperature magnetic structure, i.e. the ones that have a magnetic transition above room temperature and are measured at 5 K. At room temperature, they still have the low-temperature structure and they keep it during the rapid cooling to 5 K.

Figure 9 presents the same results as figure 8(b) but with different symbols for the HTM and LTM samples.

The following observations can be made from figure 9 when comparing KKR-CPA and VASP predictions with experimental findings:

- (1) For the HTM alloys, the decreasing trend of the magnetization as a function of the concentration of Pd is reproduced by both the disordered fcc SQSs obtained using DFT simulations and the KKR-CPA calculations.
- (2) However, the LTM phases are not reproduced by any of the calculations.

(3) The lattice constants of figure 6(b) were measured at room temperature.

The decrease of the average magnetic moment per atom with an increase of Pd content in the HTM phase can be explained by two reasons. First, Pd is a non-magnetic element and the increase of its composition decreases the average magnetic moment of an alloy. Second, the average magnetic moment in CCF_yN and CCFN-Pd_x alloys depends on the relative difference in Cr content. Similar to Fe–Cr–Ni alloys [8], Cr atoms prefer their magnetic moments to be aligned antiferromagnetically with respect to moments of other elements and their magnitudes increase with a decrease of Cr content. The LTM phase can be the low-temperature phase mentioned in [23] only detected by atom probe, thus at temperature close to 80 K.

Furthermore, the difference between the experimental and the calculated values of m_{atom} can be attributed to the presence of additional phases as observed by diffraction investigations [22]. It is interesting to note that according to figure 2, the alloys with about 20 at% of Pd, e.g. close to equimolar compositions, have a ferromagnetic to paramagnetic transition close to 300 K. From the results presented above, it is not possible to unambiguously determine which phase is the magnetic one out of the three suggested in [23], CCFN-rich, FeCoCr-rich, and FeCrPd-rich. As the presence of Cr has been found to decrease the magnetic moments, it might be conjectured that the FeCoCr-rich phase is the HTM phase mentioned above. Such a phase has earlier been found to exist in an AlCoCrCuFeNi alloy [47, 50].

The LTM phase can thus be the FeCrPd-rich phase observed in [23] and mostly detected by atom probe at very low temperature. To this end, VASP calculation was performed for a $\text{Co}_4\text{Cr}_8\text{Fe}_8\text{Ni}_4\text{Pd}_8$ SQS, thus richer in Cr, Fe, and Pd. The VASP calculation for the FeCrPd-rich configuration reproduced the experimental values for the lattice constant of the second phase in table 2 and for the average magnetic moment per atom of the LTM phase, as presented in figures 10(a) and (b).

5. Conclusions

The comparison between the experimental and calculation results of the lattice constants and average magnetic moment per atom by both the KKR-CPA and the DFT calculations with the VASP agree in that the structure of CCF_yN is well described by ordered fcc configurations.

The values of local magnetic moments on Fe, Co, Cr, and Ni atoms depend not only on the Pd concentration but on chemical disordering. Indeed, the lattice parameter was found to be very sensitive to the local atomic arrangement and this behavior has a significant effect on magnetic interactions.

The electronic structure calculations on model single-phase disordered fcc alloys predict the decreasing trend of the magnetic moment with Pd content that is in line with experimental data at 5 K up to equimolar composition and at 300 K above. This trend is not observed in the case of ordered alloys. Furthermore, the experimental values above the equimolar composition at 5 K are not satisfactorily reproduced by any of the calculations.

The divergence between experimental and calculated values can be related to the variation of the ferromagnetic to paramagnetic transition temperature as a function of palladium content and to the existence of several additional phases, e.g. FeCoCr-rich and FeNiPd-rich, observed by diffraction and detected by microscopy and atom probe investigations. Furthermore, VASP calculation for an FeCrPd-rich phase, $\text{Co}_4\text{Cr}_8\text{Fe}_8\text{Ni}_4\text{Pd}_8$ SQS, reproduced the lattice constant of the second phase identified by diffraction.

An important conclusion of this work is that the combined analysis of electronic, structural, and magnetic properties plays an important role in understanding the complexity of magnetic HEAs.

Acknowledgments

The authors are thankful to Zhaoyuan Leong and Russell Goodall of Sheffield University for the synthesis of the samples and to Institute Laue-Langevin, Grenoble, France, for awarding beam-time on the D20 and D2B diffractometers at the ILL reactor. The present work has been carried out within the FP7 European project AccMet of the Seventh Framework Programme: NMP - 2010-4.0-3, 263206. DNM would like to acknowledge the International Fusion Energy Research Centre (IFERC) for providing access to a supercomputer (Helios) at the Computational Simulation Centre (CSC) at Rokkasho (Japan). JSW would like to acknowledge the support from the Foundation for Polish Science (No. Homing/2016-1/12). The simulations were partially carried out by JSW with the support of the Interdisciplinary Centre for Mathematical and Computational Modelling (ICM), University of Warsaw, under grant no GA65-14. JT also acknowledges the support from the Polish National Science Center (No. UMO-2015/17/B/ST3/01204) and the Polish Ministry of Science and Higher Education.

References

- [1] Zhang Y, Zuo T T, Tang Z, Gao M C, Dahmen K A, Liaw P K and Lu Z P 2014 Microstructures and properties of high-entropy alloys *Prog. Mater. Sci.* **61** 1
- [2] Tsai M H and Yeh J W 2014 High-entropy alloys: a critical review *Mater. Res. Lett.* **2–3** 107
- [3] Koželj P, Vrtnik S, Jelen A, Jazbec S, Jagličić Z, Maiti S, Feuerbacher M, Steurer W and Dolinšek J 2014 Discovery of a superconducting high-entropy alloy *Phys. Rev. Lett.* **113** 107001
- [4] Jasiewicz K, Wiendlocha B, Korbeń P, Kaprzyk S and Tobola J 2016 Superconductivity of $\text{Ta}_{34}\text{Nb}_{33}\text{Hf}_8\text{Zr}_{14}\text{Ti}_{11}$ high-entropy alloy from first principles calculations *Phys. Status Solidi* **10** 415
- [5] Yeh J W, Chen S K, Lin S J, Gan J Y, Chin T S, Shun T T, Tsau C H and Chang S Y 2004 Nanostructured high-entropy alloys with multiple principal elements: novel alloy design concepts and outcomes *Adv. Eng. Mater.* **6** 299
- [6] Lu Z P, Wang H, Chen M W, Baker I, Yeh J W, Liu C T and Nieh T G 2015 An assessment on the future development of high-entropy alloys: summary from a recent workshop *Intermetallics* **66** 67

- [7] Lu Y, Dong Y, Jiang L, Wang T, Li T and Zhang Y 2015 A criterion for topological close-packed phase formation in high-entropy alloys *Entropy* **17** 2355
- [8] Toda-Caraballo I and Rivera-Díaz-del-Castillo P E L 2016 A criterion for formation of high-entropy alloys based on lattice distortion *Intermetallics* **71** 76
- [9] Otto F, Yang Y, Bei H and George E P 2013 Relative effects of enthalpy and entropy on the phase stability of equiatomic high-entropy alloys *Acta Mater.* **61** 2628
- [10] Miracle D B, Miller J D, Senkov O N, Woodward C, Uchic M D and Tiley J 2014 Exploration and development of high-entropy alloys for structural applications *Entropy* **16** 494
- [11] Guo S, Ng C, Lu J and Liu C T 2011 Effect of valence electron concentration on stability of fcc or bcc phases in high entropy alloys *J. Appl. Phys.* **109** 103505
- [12] Guo S, Ng C, Wang Z and Liu C T 2014 Solid solutioning in equiatomic alloys: limit set by topological instability *J. Alloys Compd.* **583** 410
- [13] Poletti M G and Battezzati L 2014 Electronic and thermodynamic criteria for the occurrence of high-entropy alloys in metallic systems *Acta Mater.* **75** 297
- [14] Singh A K, Kumar N, Dwivedi A and Subramaniam A 2014 A geometrical parameter for the formation of disordered solid solutions in multi-component alloys *Intermetallics* **53** 112
- [15] Ye Y F, Wang Q, Lu J, Liu C T and Yang Y 2015 Design of high-entropy alloys: a single-parameter thermodynamic rule *Scr. Mater.* **104** 53
- [16] Ye Y F, Liu C T and Yang Y 2015 A geometric model for intrinsic residual strain and phase stability in high-entropy alloys *Acta Mater.* **94** 152
- [17] Wang Z, Qiu W, Yang Y and Liu C T 2015 Atomic-size and lattice-distortion effects in newly developed high-entropy alloys with multiple principal elements *Intermetallics* **64** 63
- [18] Senkov O N and Miracle D B 2016 A new thermodynamic parameter to predict formation of solid solution or intermetallic phases in high-entropy alloys *J. Alloys Compd.* **658** 603
- [19] Cornide J et al 2015 Structure and properties of some CoCrFeNi-based high-entropy alloys *The Minerals, Metals & Materials Society, TMS2015 Supplemental Proc.* (New York: Wiley) (http://dx.doi.org/10.1007/978-3-319-48127-2_139)
- [20] Dahlborg U, Cornide J, Calvo-Dahlborg M, Hansen T C, Leong Z, Asensio Dominguez L, Chambrelan S, Cunliffe A, Goodall R and Todd I 2015 Crystalline structures of some high-entropy alloys obtained by neutron and x-ray diffraction *Acta. Phys. Pol. A* **128** 552
- [21] Cornide J, Calvo-Dahlborg M, Chambrelan S, Asensio Dominguez L, Leong Z, Dahlborg U, Cunliffe A, Goodall R and Todd I 2015 Combined atom probe tomography and TEM investigations of CoCrFeNi, CoCrFeNi-Pd_x ($x = 0.5, 1.0, 1.5$) and CoCrFeNi-Sn *Acta Phys. Pol. A* **128** 557
- [22] Dahlborg U, Cornide J, Calvo-Dahlborg M, Hansen T C, Fitch A, Leong Z, Chambrelan S and Goodall R 2016 Structure of some CoCrFeNi and CoCrFeNiPd_x multicomponent HEA alloys by diffraction techniques *J. Alloys Compd.* **681** 330
- [23] Calvo-Dahlborg M, Cornide J, Dahlborg U, Chambrelan S, Hatton G D and Fones A 2017 Structural and microstructural characterization of CoCrFeNiPd high-entropy alloys *Solid State Phenom.* **257** 72
- [24] Kourov N I, Pushin V G, Korolev A V, Knyazev Yu V, Ivchenko M V and Ustyugov Yu M 2015 Peculiar features of physical properties of the rapid quenched AlCrFeCoNiCu high-entropy alloy *J. Alloys Compd.* **636** 304
- [25] Zhang K B, Fu Z Y, Zhang J Y, Shi J, Wang W M, Wang H, Wang Y C and Zhang Q L 2010 Annealing on the structure and properties evolution of the CoCrFeNiCuAl high-entropy alloy *J. Alloys Compd.* **502** 295
- [26] Kao Y F, Chen S K, Chen T J, Chu P C, Yeh J W and Lin S J 2011 *J. Alloys Compd.* **509** 1607
- [27] Lucas M S, Mauger L, Muñoz J A, Xiao Y, Sheets A O, Semiatin S L, Horwath J and Turgut Z 2011 Magnetic and vibrational properties of high-entropy alloys *J. Appl. Phys.* **109** 07E307
- [28] Lucas M S et al 2013 Thermomagnetic analysis of FeCoCr_xNi alloys: magnetic entropy of high-entropy alloys *J. Appl. Phys.* **113** 17A923
- [29] Kozak R, Sologubenko A S and Steurer W 2014 Single-phase high-entropy alloys—an overview *Z. Kristallogr.* **230** 55
- [30] Calvo-Dahlborg M, Cornide J, Richomme F, Jouen S and Juraszek J 2017 in preparation
- [31] Körmann F, Ma D, Belyea D D, Lucas M S, Miller C W, Grabowski B and Sluiter M H F 2015 Treasure maps for magnetic high-entropy-alloys from theory and experiment *Appl. Phys. Lett.* **107** 142404
- [32] Niu C, Zaddach A J, Oni A A, Sang X, Hurt J W III, LeBeau J M, Koch C C and Irving D L 2015 Spin-driven ordering of Cr in the equiatomic high-entropy alloy NiFeCrCo *Appl. Phys. Lett.* **106** 161906
- [33] Tamm A, Aabloo A, Klintenberg M, Stocks M and Caro A 2015 Atomic-scale properties of Ni-based FFC ternary and quaternary alloys *Acta Mater.* **99** 307
- [34] Niu C, Zaddach A J, Koch C C and Irving D L 2016 First principles exploration of near-equiatomic NiFeCrCo high-entropy alloys *J. Alloys Compd.* **672** 510
- [35] Leong Z, Wróbel J S, Dudarev S L, Goodall R, Todd I and Nguyen-Manh D 2017 The effect of electronic structure on the phases present in high-entropy alloys *Sci. Rep.* **7** 39803
- [36] Bansil A, Kaprzyk S, Mijnders P E and Tobola J 1999 *Phys. Rev. B* **60** 13396
- [37] Stopa T, Kaprzyk S and Tobola J 2004 *J. Phys.: Condens. Matter* **16** 4921
- [38] Kaprzyk S and Bansil A 1990 *Phys. Rev. B* **42** 7358
- [39] Kresse G and Furthmüller J 1996 *Comput. Mater. Sci.* **6** 15
- [40] Kresse G and Furthmüller J 1996 Efficient iterative schemes for *ab initio* total-energy calculations using a plane-wave basis set *Phys. Rev. B* **54** 11169
- [41] Perdew J P, Burke K and Ernzerhof M 1997 *Phys. Rev. Lett.* **78** 1396
- [42] Monkhorst H J and Pack J D 1976 *Phys. Rev. B* **13** 5188
- [43] Zunger A, Wei S, Ferreira L G and Bernard J E 1990 *Phys. Rev. Lett.* **65** 353
- [44] van de Walle A, Tiwary P, de Jong M, Olmsted D L, Asta M, Dick A, Shin D, Wang Y, Chen L Q and Liu Z 2013 *Calphad* **42** 13
- [45] van de Walle A, Asta M and Ceder G 2002 *Calphad* **26** 539
- [46] Wróbel J S, Nguyen-Manh D, Lavrentiev M Y, Muzyk M and Dudarev S L 2015 *Phys. Rev. B* **91** 024108
- [47] Laurent-Brocq M, Akhatova A, Perrière L, Chebini S, Sauvage X, Leroy E and Champion Y 2015 Insights into the phase diagram of the CrMnFeCoNi high-entropy alloy *Acta Mater.* **88** 355
- [48] Santodonato L J, Zhang Y, Feyngenson M, Parish C M, Gao M C, Weber J K, Neufeind J C, Tang Z and Liaw P K 2015 Deviation from high-entropy configurations in the atomic distributions of a multi-principal-element alloy *Nat. Commun.* **6** 5964
- [49] Lavrentiev M Yu, Wrobel J S, Nguyen-Manh D and Dudarev S L 2014 Magnetic and thermodynamic properties of face-centered cubic Fe–Ni alloys *Phys. Chem. Chem. Phys.* **16** 16049
- [50] Singh S, Wanderka N, Kiefer K, Siemensmeyer K and Banhart J 2011 Effect of decomposition of the Cr–Fe–Co rich phase of AlCoCrCuFeNi high-entropy alloy on magnetic properties *Ultramicroscopy* **111** 619